

# 量子赛道跑出“中国速度”

## ——“解读量子计算新进展”系列报道之三

◎本报记者 洪敬谱 吴长锋

量子计算机理论上具备超越经典计算机的计算能力,正在引领新一代计算技术。

量子芯片是量子计算机的核心处理器。近年来,我国在量子芯片领域取得积极进展,在全球量子赛道中跑出了“中国速度”。

### 成果频出

目前,量子计算比较主流的技术路线包括超导、光量子、离子阱、中性原子和硅半导体等。这些量子体系各具特点,目前仍处于“百家争鸣”状态。

中电信量子信息科技集团有限公司(以下简称“中电信量子集团”)量子计算技术部牵头人孙汉涛认为,超导量子芯片的技术发展路线比较成熟,主要优势是与现有半导体工业技术高度兼容,可设计性高,易于耦合,量子门操作速度快。

2019年,谷歌公司成功研制出具有53个量子比特的量子芯片“悬铃木”(Sycamore)。基于该芯片,100万次量子随机线路采样耗时约200秒,而当时世界排名第一的超级计算机则需要1万年左右。谷歌公司宣称实现了量子优越性,这被视为量子计算发展史上的重要时刻。

2020年,由中国科学院院士、中国科

学技术大学(以下简称“中科大”)教授潘建伟领衔的陆朝阳教授课题组和中国科学院上海微系统与信息技术研究所等单位合作,构建了光量子计算原型机“九章”,求解了最高达76个光子的高斯玻色采样问题,求解速度超越经典超级计算机。“九章”在国际上首次实现基于光学体系的量子计算优越性,使中国成为全球第二个实现量子优越性的国家。随后发展的“九章三号”,能操纵255个光子。“九章三号”1微秒可算出的最复杂样本,用世界上最强大的超级计算机之一“前沿”(Frontier)来计算,约需200亿年。

2021年,潘建伟团队构建的66个量子比特可编程超导量子计算原型机“祖冲之二号”,执行量子随机线路采样任务的速度比当时全球最快的超级计算机快1000万倍以上,计算复杂度比“悬铃木”提高了6个数量级。

2024年12月17日,我国超导量子计

结果表明,“祖冲之三号”超导量子计算芯片有105个超导量子比特,在各种性能指标上与谷歌公司的量子芯片“威洛”(Willow)旗鼓相当。目前,研究团队正基于“祖冲之三号”超导量子计算芯片开展相关测试工作,为实现大规模的量子纠错和量子比特操控铺平道路。

### 优势显现

当前,高能量子芯片数量并不多,且超导量子计算芯片还需要室温电子学系统、低温传输线缆、稀释制冷机等配套硬件设备维持其运行。

为了使更多量子计算算法、软件开发工作者,以及量子计算爱好者接触到量子计算,我国科学家及技术人员通过云技术,为大众提供量子计算便利。

2024年1月6日,由本源量子计算科技(合肥)股份有限公司(以下简称“本源量子”)自主研发的超导量子计算机“本源悟空”上线运行。“本源悟空”搭载的72位自主超导量子芯片“悟空芯”,是本源量子自主研发的第三代超导量子芯片。“本源悟空”可一次性下发现,执行多达200个量子线路的计算任务,相较于只能同时下发现、执行单个量子线路的国际同类量子计算机,具有更大速度优势。“本源悟空”已为全球139个国家和地区的超1800万用户,完成30余万个量子计算任务。”安徽省量子计算工程研究中心副主任、“本源悟空”云服务研制团队负责人赵雪娇告诉记者。

目前,我国科学家已在教育、生物医药等多个领域推广应用量子算力。2024年12月8日,我国首个量子计算与数据医学研究院——合肥量子计算与数据医学研究院在本源量子成立。该研究院由蚌埠医科大学和本源量子共同设立,致力于通过量子计算提升我国医疗数据的安全性和应用效能。

“在生物医药行业,量子计算能够在药物设计、蛋白质结构预测、医疗数据的分析与处理等领域提供助力。”赵雪娇说。

2024年4月,中国科学院量子信息与量子科技创新研究院向科大国盾量子技术股份有限公司(以下简称“国盾量子”)交付一款504比特超导量子计算芯片“晓鸿”,用于验证国盾量子自主研发的千比特操控系统等核心硬件。当年12月,基于“晓鸿”芯片,中电信量子集团和国盾量子联合研发出国内单台比特数最多的超导量子计算机“天衍504”,并接入中国



图为河南郑州网络安全科技馆的量子计算机知识展区。

马健/视觉中国供图

电信“天衍”量子计算云平台。该平台自2023年11月对外服务以来,已为来自全球50多个国家和地区的用户,提供超过60万个实验任务的计算服务。

### 未来可期

多位受访专家认为,当前,包括量子芯片在内的量子计算技术仍处于早期研发阶段,离实际应用还有很长的路要走。但是,科学家们对量子科技发展充满信心。

“国际公认的量子计算发展路线分为三步,第一步是实现量子计算优越性,这一目标中国、美国等国家已达到;第二步是实现专用的量子模拟机;第三步是在实现量子纠错的基础上,构建可编程通用量子计算机。”孙汉涛说。

目前,研究人员正在努力实现量子计算的第二个目标,已经取得一系列进展。例如,中国科大研究团队构建的超冷原子量子模拟器“天元”,以超越经典计算机的模拟能力首次验证了该体系中的反铁磁相变。

2024年9月,安徽省气象局、中国电信股份有限公司安徽分公司、中电信量子集团签署战略合作协议,三方未来将持续发挥各自资源优势,共同协助安徽

气象局构建全国领先的气象信息基础设施能力基座,提升其在信息服务、数据创新应用、数据安全、防灾减灾等方面的工作质效。

在孙汉涛看来,此次签约意味着量子计算在气象预测领域的应用迈出重要一步,将开创降雨精准预测新范式。未来,量子科技有望改善灾害预警系统,助力人类更好应对天气变化,减少经济损失。

“经典计算机在开发数值天气和气候预测模型时存在局限性,‘天衍’量子计算云平台为算法训练提供相关计算资源支撑,可以帮助气象工程师、环境科学等专业人员获得更及时、精准的数据。”孙汉涛说。

孙汉涛认为,未来5年里,量子计算有可能在一些实际应用场景里体现出真正优越性。“量子计算最有可能的应用是在化学领域,用于模拟化学分子结构、化学反应等,实现更高效、更低耗能的化学品设计。”孙汉涛说。

孙汉涛进一步展望,预计未来3到5年,研究人员可以实现数百至上千个量子比特的相干操纵,实现可扩展的量子纠错;未来10到15年,在量子纠错的基础上,有可能构建具备基本功能的通用量子计算机,探索量子计算在化学模拟、加密破解、大数据分析等方面的应用。

# 碳化硅集成光量子纠缠器件领域研究获突破

科技日报讯 (记者罗云鹏 通讯员李晓慧)记者从哈尔滨工业大学(深圳)获悉,该校教授宋清海、周宇团队在碳化硅集成光量子纠缠器件领域取得新突破,将进一步推进集成光量子信息技术在量子网络和量子传感领域的应用。相关论文近日发表于《自然·通讯》。

研究团队在绝缘体上的碳化硅材料

上制备出单个电子自旋阵列,并通过精细操控展示了这些自旋的相干特性。

同时,研究团队将特殊的碳化硅外延层晶圆与氧化硅晶圆结合,通过磨削和抛光技术将碳化硅层减薄到200纳米。

随后,研究团队利用离子注入技术,在碳化硅层中引入双空位自旋,并通过光磁共振(ODMR)技术验证了自旋相干特

性。据悉,在此次研究的碳化硅中,约有1.1%的碳原子和4.7%的硅原子具有核自旋特性。

宋清海介绍:“我们成功识别了一种特定类型的碳化硅量子缺陷,发现核自旋与电子自旋之间的强耦合能够实现快速的量子操作。”这些发现为碳化硅片上集成的光量子信息处理提供重要基础。

另悉,研究团队将这种电子—核纠缠量子寄存器集成到光波导中后,成功实现了接近100%的核自旋极化,并制备出最大纠缠贝尔态。

周宇说,该实验结果表明,量子寄存器的光发射和自旋在集成后保持稳定,纠缠也能够稳定保持在室温的光波导中。

# 新技术为隔空充电提供更多可能

◎本报记者 王禹涵

飞行中的无人机、正在移动的智能机器人,都可以远程隔空充电,科幻小说里描述的场景有望成为现实。

近日,由西安电子科技大学教授李龙课题组与中国科学院院士、东南大学教授崔铁军课题组共同研发的一种自适应无线传能技术,可以用类似Wi-Fi的无线传输方式,将无线能量实时、高效地聚焦并传输到动态的终端设备上,实现无电池供电的感知、计算和通信。

在李龙看来,这项研究是面向无线传能、感知、通信一体化领域的探索,未来有望为万物智联的传感器设备进行无线供电。相关论文发表于《自然·通讯》。

### 边移动边充电

无人机广泛应用于高空拍摄、物流配送、农业植保、应急救援等诸多领域,机器人、可穿戴设备等智能硬件也走进人们的生活,但续航能力却始终制约其

进一步发展。如何为这些智能设备提供可靠、持久的能源供给,成为亟待解决的技术难题。

无线能量传输技术的突破,意味着未来的智能设备有望摆脱传统电池和线充电设施。

“我们针对精确近场无线定位、自适应无线能量传输、高效无线能量收集等问题,构建了一种基于双频超表面、卷积神经网络近场定位的自适应无线传能网络。它能进行同步的目标感知定位和波束调控,进而实现自适应追踪的无线能量传输。”李龙说,这项研究在动态无线能量传输和无线定位领域取得突破性进展。

据了解,传统的无线充电技术主要依赖于近距离、接触式的电磁谐振感应,其效率和适用范围受到空间、距离、环境、设备等制约。

李龙课题组研究的基于电磁超表面的辐射式无线能量传输与接收技术有望突破这一瓶颈。这种技术宛如“智慧大脑”,它能通过目标感知和环境交互实现智能化调整电磁波传输参数,并根据周围环境变化及设备实时需求,由此对射频能量进行高效收集和直流转换,

设备输送能量。

与传统的无线充电方式相比,自适应追踪的无线能量传输技术有望支持无人机、智能机器人等终端设备,在移动过程中进行稳定、高效的非接触式无线充电。团队成员、西安电子科技大学博士生夏得校说,这项技术是电磁超表面在无线传能领域的创新和突破,促进信息超表面研究沿着智能化、多功能方向发展。

### 厘米级跟踪定位

如何精准定位移动中的智能设备?这是实现远程隔空充电的关键。

研究人员将超表面能量接收整流过程中产生的二阶谐波作为定位信号进行反馈,结合超表面时空编码技术和卷积神经网络,首次在单发单收系统上实现了3厘米分辨率的近场定位精度。

研究人员介绍,他们构建了一款双频共口径的可编程超表面,用于实现全双工的辐射调控和目标感知。他们还设计了用于无线供电的传感器终端,由此对射频能量进行高效收集和直流转换,具有应用潜力。

实现无电池的环境数据感知和计算,并将感知的数据通过蓝牙进行上传。最终,研究人员利用双频超表面上的阵列,对来自终端设备的定位信号进行时空编译码调制。在前期完成网络训练的基础上,通过卷积神经网络终端实现快速分类及精确获取位置信息。

夏得校说,在这一系统中,超表面不仅能实现精确的目标定位,还能根据实时变化的环境和目标,进行灵活的能量聚集,实现跟踪式隔空输能。

无线充电技术的前景广阔,随着规模化生产和技术创新迭代,其应用成本也将逐步降低。经济实惠的无线充电技术,可为大型智能仓储、可植入医疗设备及低空经济等领域提供更便捷的充电解决方案。

“我们的研究通过引入信息超材料技术,为非接触式设备能量信息同传提供了一套高效且可行的解决方案。这一探索不仅能拓宽学术视野,更有望加速无线充电技术在未来应用场景中的实践与普及。”李龙说,自适应无线传能技术将推动6G物联网、信息超表面、智能无人机等行业的发展,具有应用潜力。

## K 新知

# 太阳迷你暗条爆发机制揭示

科技日报讯 (记者赵汉斌)记者1月13日从中国科学院云南天文台获悉,该台研究人员利用一米新真空太阳望远镜和太阳动力学天文台获取的数据,详细研究了太阳活动区中一个三维扇—脊磁型中由两步磁重联触发的迷你暗条间歇性爆发,并取得了重要进展。这一研究对理解太阳活动区的物理过程具有重要意义,相关论文发表于《天体物理学报》。

迷你暗条是大尺度暗条的类似物,其空间尺度较小,寿命较短,但发生率较高。它们多数位于宁静区,少数位于活动区或冕洞,其爆发常伴随喷流和环形耀斑的产生。此次研究中,该团队发现,迷你暗条的爆发与扇—脊结构内的两步磁重联过程密切相关。在太阳物理学中,磁重联被认为是驱动太阳活动(如太阳耀斑、日冕加热等)的重要机制之一。

通过对2023年4月7日至8日活动区NOAA 13272中位于扇—脊磁型内的一个迷你暗条两次间歇性爆发的详细分析,研究人员发现,两次爆发都与扇—脊结构内的两步磁重联过程相关。第一次磁重联发生在小尺度磁环和内脊之间,导致内脊重构。当重构后的内脊逐渐向外脊靠近时,它们在磁零点处发生了第二次磁重联,导致迷你暗条部分爆发。随后,这种两步磁重联过程再次发生,触发迷你暗条完全爆发。

研究认为,两步磁重联是触发迷你暗条两次爆发的主要机制,其中零点磁重联是迷你暗条爆发的直接触发者。磁场外推的结果也进一步证实了一个三维零点的扇—脊结构的存在。该研究详细分析了日冕零点磁重联前及磁重联期间扇—脊结构内外脊的演化过程,并解释了迷你暗条爆发前零点磁重联的触发机制,揭示了零点磁重联与迷你暗条爆发之间的因果关系。

# 超分子阿基米德多面体构筑有了新途径

科技日报讯 (记者陈曦 通讯员赵晖)记者1月13日从天津大学获悉,该校理学院教授胡文平、王雨、吴煌与诺贝尔化学奖获得者詹姆斯·弗雷泽·司徒塔特团队联手开辟了光电小分子手性组装新途径,构筑了超分子扭棱立方体,在光电功能的手性阿基米德多面体构筑上取得突破。相关论文发表于《自然》。

2000多年前,古希腊数学家阿基米德提出了13种以结构复杂著称的阿基米德多面体。长期以来,阿基米德多面体备受数学家、化学家、材料学家关注。这一领域的相关研究可对新材料、生物医药、化学化工等领域产生深远影响。比如,许多球形病毒衣壳和铁蛋白展现出类似阿基米德多面体的拓扑结构。如果能设计并合成超分子扭棱立方体,将为理解球形生物大分子在生物系统中的形成与功能执行提供重要途径。

在13种阿基米德多面体中,扭棱立方体具有拓扑手性。拓扑手性描述的是一种分子或物体的结构特性,这种特性使它们与其镜像在三维空间中无法直接重合,就像人们的左右手一样,各有各的形状,各有各的“个性”。实现扭棱立方体的立体特异性构筑一直是化学家和材料学家追求的目标。

联合研究团队基于光电功能分子,设计并合成了“8”字形的螺旋大环,并通过螺旋大环之间的144个弱氢键实现了超分子扭棱立方体的定向组装。胡文平介绍,该研究实现了左手扭棱立方体和右手扭棱立方体的选择性构筑。由于其独特的多孔结构,该扭棱立方体能够同时装载多个不同的有机客体分子,还能在立方体的内部空腔和外部“口袋”中选择性地装载不同的客体分子。

该扭棱立方体还表现出优异的光电性能,能在光照下发生可逆的颜色变化。研究人员可以用光照来调节其弹性和硬度,为开发机械性能可调的先进光电功能材料奠定基础。这项研究还为构筑具有拓扑手性的手性多面体提供了全新组装途径,为开发具有丰富包裹性能的智能人工多面体提供了新方向。此外,在模拟生物封装材料这一方向,该研究也迈出重要一步,为设计先进的光电功能晶态材料提供了新思路。

# 浙江上山遗址

## 发现东亚最早酒类酿造证据

科技日报讯 (记者陆成宽)酿酒技术何时起源、如何发展,一直是未解之谜。记者日前获悉,中国科学院地质与地球物理研究所、浙江省文物考古研究所及美国斯坦福大学的科研人员,聚焦我国浙江上山文化遗存,利用多种微体化石分析技术,发现了东亚最早酒类酿造证据,揭示了上山遗址1万年前稻米酿酒技术。相关论文在线发表于《美国国家科学院院刊》。

科研人员在浙江省浦江县上山遗址采集了12件陶器残片。这些陶器的用途分别为发酵、烹饪等。“样本采集后,我们对陶器的内表面残留物、陶胎、文化层沉积物等进行微体化石提取与分析,以确定陶器的使用功能和相应的食物加工方式。”论文第一作者、美国斯坦福大学教授刘莉介绍。

植硅体分析显示,陶器残留物和陶胎含有大量驯化稻的植硅体。这意味着稻米是上山人群的重要植物资源。同时,这也说明,当时稻壳和稻叶被用于陶器制作,进一步证明稻米在上山文化中的核心地位。

科研人员还在陶器残留物中发现了稻米、稗草等多种植物的淀粉粒。“较多淀粉粒表现出酶水解和糊化的现象,这一迹象表明,这些植物曾经被发酵过。我们进一步研究发现了大量真菌成分,如红曲霉和酵母细胞,其中一些显示出典型的生长发育阶段特点。这些真菌与传统酿造曲酒时使用的真菌种类相关,如红曲霉是中国传统红曲酒酿造使用的主要霉菌。”刘莉说。

紧接着,科研人员分析了红曲霉和酵母遗存在不同陶器类型的分布,发现小口罐中红曲霉和酵母的数量显著高于用作炊器的罐和用来加工一般食物的大口盆。这表明,陶器类型与特定功能相关,小口罐可能专门用于酿造发酵酒。

刘莉认为,这项研究不仅揭示了早期稻米酿酒的复杂性与创新性,也为理解东亚地区稻作农业的起源、早期社会结构和技术传播提供了重要科学依据。



# Room-temperature waveguide integrated quantum register in a semiconductor photonic platform

Received: 11 September 2024

Accepted: 13 November 2024

Published online: 26 November 2024

Check for updates

Haibo Hu<sup>1,2,10</sup>, Yu Zhou<sup>1,3,10</sup>✉, Ailun Yi<sup>1,4,5,10</sup>✉, Tongyuan Bao<sup>1</sup>, Chengying Liu<sup>1</sup>, Qi Luo<sup>1</sup>, Yao Zhang<sup>1</sup>, Zi Wang<sup>1</sup>, Qiang Li<sup>6,7</sup>, Dawei Lu<sup>1,3,8</sup>, Zhengtong Liu<sup>1,2</sup>, Shumin Xiao<sup>1,2,3,9</sup>, Xin Ou<sup>1,4,5</sup>✉ & Qinghai Song<sup>1,2,3,9</sup>✉

Quantum photonic integrated circuits are reshaping quantum networks and sensing by providing compact, efficient platforms for practical quantum applications. Despite continuous breakthroughs, integrating entangled registers into photonic devices on a CMOS-compatible platform presents significant challenges. Herein, we present single electron-nuclear spin entanglement and its integration into a silicon-carbide-on-insulator (SiCOI) waveguide. We demonstrate the successful generation of single divacancy electron spins and near-unity spin initialization of single <sup>13</sup>C nuclear spins. Both single nuclear and electron spin can be coherently controlled and a maximally entangled state with a fidelity of 0.89 has been prepared under ambient conditions. Based on the nanoscale positioning techniques, the entangled quantum register has been further integrated into SiC photonic waveguides for the first time. We find that the intrinsic optical and spin characteristics of the register are well preserved and the fidelity of the entangled state remains as high as 0.88. Our findings highlight the promising prospects of the SiCOI platform as a compelling candidate for future scalable quantum photonic applications.

Nuclear-electron quantum registers are essential components of multi-node quantum networks<sup>1,2</sup> and quantum sensing<sup>3–5</sup>. These registers, with electron-coupled nuclear spins serving as memory qubits or sensors, play a crucial role in network operations<sup>1,2,5</sup>. Color centers in diamonds have been at the forefront of constructing quantum networks, with significant advancements and achievements realized over

the past decades with two main approaches<sup>1,2,6–10</sup>. The first approach entails the entanglement of nitrogen-vacancy centers in bulk diamonds at distant sites using herald protocols<sup>1,6–8</sup>. A more integrated strategy incorporates silicon vacancy<sup>9</sup> and proximal nuclear spins<sup>2</sup> within diamond nanophotonics, marking significant steps in quantum network construction. At the same time, quantum sensing using

<sup>1</sup>Ministry of Industry and Information Technology Key Lab of Micro-Nano Optoelectronic Information System, Guangdong Provincial Key Laboratory of Semiconductor Optoelectronic Materials and Intelligent Photonic Systems, Harbin Institute of Technology, Shenzhen, China. <sup>2</sup>Pengcheng Laboratory, Shenzhen, China. <sup>3</sup>Quantum Science Center of Guangdong-HongKong-Macao Greater Bay Area (Guangdong), Shenzhen, China. <sup>4</sup>State Key Laboratory of Materials for Integrated Circuits, Shanghai Institute of Microsystem and Information Technology, Chinese Academy of Sciences, Shanghai, China. <sup>5</sup>The Center of Materials Science and Optoelectronics Engineering, University of Chinese Academy of Sciences, Beijing, China. <sup>6</sup>Institute of Advanced Semiconductors, Zhejiang Provincial Key Laboratory of Power Semiconductor Materials and Devices, ZJU-Hangzhou Global Scientific and Technological Innovation Center, Hangzhou, Zhejiang, China. <sup>7</sup>State Key Laboratory of Silicon Materials and Advanced Semiconductors & School of Materials Science and Engineering, Zhejiang University, Hangzhou, China. <sup>8</sup>Shenzhen Institute for Quantum Science and Engineering and Department of Physics, Southern University of Science and Technology, Shenzhen, China. <sup>9</sup>Collaborative Innovation Center of Extreme Optics, Shanxi University, Taiyuan, Shanxi, China. <sup>10</sup>These authors contributed equally: Haibo Hu, Yu Zhou, Ailun Yi. ✉e-mail: [zhouyu2022@hit.edu.cn](mailto:zhouyu2022@hit.edu.cn); [ouxin@mail.sim.ac.cn](mailto:ouxin@mail.sim.ac.cn); [qinghai.song@hit.edu.cn](mailto:qinghai.song@hit.edu.cn)

defects in diamonds has advanced significantly, finding applications across diverse areas and demonstrating considerable development<sup>11</sup>. To date, defect-based quantum systems are rapidly emerging as one of the cornerstones for the next generation of integrated quantum networking and sensing. Despite significant advancements in these quantum technologies, achieving a fully integrated quantum photonic network chip with substantial volume and energy advantages remains a formidable challenge. The primary difficulty lies in integrating entangled registers into photonic devices on a CMOS-compatible platform, a task that continues to pose substantial obstacles.

Silicon carbide, an emerging CMOS-compatible quantum material<sup>12–14</sup>, holds the potential to be the host for realizing a fully monolithic quantum photonic network processor<sup>15,16</sup>. This potential is attributed to the recent rapid advancements in SiC quantum registers and silicon-carbide-on-insulator (SiCOI) platforms. On the one hand, the coherence time of individual electron spins in SiC has significantly extended from milliseconds<sup>17</sup> to seconds<sup>18</sup>. Besides the electron spin, wealthy nuclear spin resources are ideal quantum memory candidates in quantum network construction<sup>8</sup>. Ensemble nuclear spins in SiC have been efficiently initialized through dynamical nuclear polarization (DNP)<sup>19</sup>. Furthermore, coherent control and entanglement of both ensemble<sup>20</sup> and individual nuclear spins<sup>21</sup> at cryogenic temperatures provides a solid foundation for many nuclear-spin involving quantum networks and sensing applications<sup>3,4,22–25</sup>. On the other hand, the advancement of quantum-grade SiCOI platforms has broadened opportunities for integrating photonic devices directly on-chip. SiCOI platforms are recognized for their versatile functionalities, attributed to the inherent nonlinear properties of SiC, including photon frequency conversion to the telecom band<sup>26</sup>, generation of entangled photon pairs<sup>27</sup>, and electro-optic modulation<sup>28</sup>. Despite continuous

breakthroughs in SiC quantum registers and the SiCOI photonic platform, integrating them into a quantum photonics platform with waveguide-integrated entangled quantum registers remains a significant challenge, leaving this area still blank. Here, we address this challenge by experimentally demonstrating the integration of single electron-nuclear spin entanglement into a SiCOI waveguide. Our findings indicate a promising approach for achieving scalable quantum photonic applications in the future.

## Results

### Generation and coherent control of single divacancy spins on SiCOI

PL6 is a relatively new type of 4H-SiC divacancy color center with attractive optical and spin properties like high brightness (150 kcps) and ODMR contrast (30%) at room temperature<sup>29</sup>. PL6 is believed to be situated within stacking faults acting as quantum wells<sup>30</sup>. This unique positioning enhances these defects' (including PL5 and PL7) stability against photo-ionization, different from the previously identified  $V_{Si}V_C$  defects (PL1-PL4)<sup>12</sup>. To maintain the key characteristics of the single divacancy color centers, the SiCOI wafer is fabricated by a thinning and polishing technique<sup>26</sup>. First, a 4H-SiC wafer with an epitaxy layer is bonded to an oxidized Si wafer. Subsequently, the bonded SiC layer is mechanically ground and then subjected to chemical-mechanical polished (CMP) to achieve a thickness of several micrometers. The SiCOI wafer with a designed thickness of 200 nm is obtained after etching the SiC layer (see Methods and Supplementary Fig. 1 for more details of the sample). The divacancy spins are generated in SiCOI via a selective carbon ion implantation, as displayed in Fig. 1a. 8 × 8 hole arrays are fabricated on the SiC layer using 180 nm thick PMMA (A4) as a photoresist through E-beam lithography (Fig. 1a). Following the

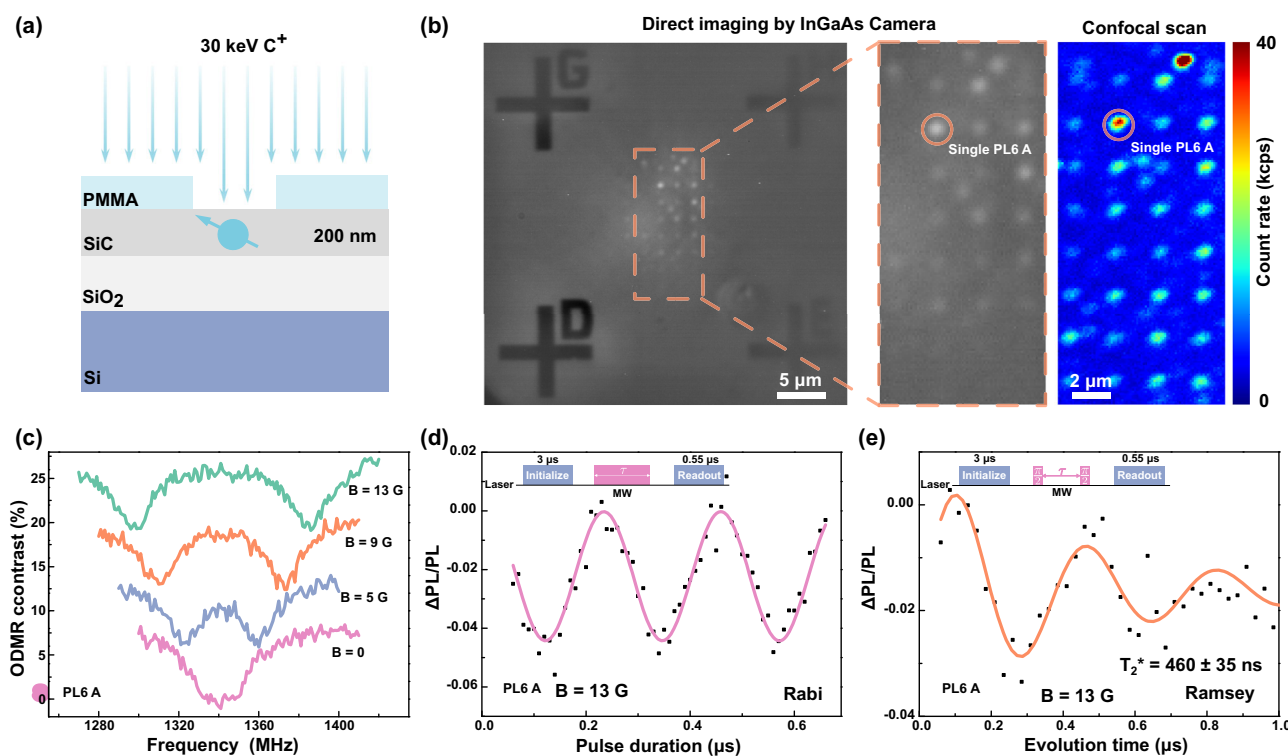


**Fig. 1 | Generation and coherent control of single color center PL6 A on SiCOI.** **a** Diagram of the cross-section view of the SiCOI sample with 30 keV  $C^+$  ion implantation through a PMMA mask with an 8 × 8 array of 100 nm diameter holes. **b** Direct and confocal scanning image of the implanted sample. The Au cross marker is deposited for nanoscale spatial positioning. PL6 A is circled in both the CCD image and the confocal scan. **c** ODMR spectra of PL6 A under varying c-axis magnetic fields, with each ODMR peak displaying a divergence at a slope of

$2.82 \pm 0.02 \text{ MHz/G}$ .  $D = 1340.4 \pm 1.3 \text{ MHz}$ ,  $E = 6.95 \pm 1.82 \text{ MHz}$  are extracted from the peaks' fitting. **d** Rabi oscillation and **e** Ramsey fringes of the PL6 A under 0.1 mW excitation. Each cycle is repeated around 10 million times to reduce the measurement error. The black dots represent the raw data, and the solid lines depict the fitting with the cosine and cosine exponential decay functions, respectively. From the fitting, the inhomogeneous spin-dephasing time  $T_2^*$  is extracted to be  $460 \pm 35 \text{ ns}$ .

30 keV Carbon ion implantation with a dose of  $7.8 \times 10^{11} \text{ cm}^{-2}$ , the sample is annealed in a high vacuum at 900 °C for 30 min to remove residual lattice damage. To characterize the defects array, a single-defect direct imaging system (Supplementary Fig. 3a) is built, and the acquired image taken by an InGaAs camera is shown in Fig. 1b. The designed defect array is clear with the same spacing length and numbers as the designed pattern (Supplementary Fig. 3b). Confocal photoluminescence scanning of the same area is then performed using off-resonant excitation at continuous wave (CW) 914 nm (Supplementary Note 1 for the setups). The two maps in Fig. 1b acquired by different imaging methods are similar, reaffirming that we have successfully generated the defect array in SiCOI as designed.

To confirm the defect type, optically detected magnetic resonance (ODMR) of the defect is performed at different B fields parallel to the c-axis. Figure 1c summarizes the results of the defect marked with a red circle in Fig. 1b. The two branches of the ODMR spectrum diverge with a slope of  $2.82 \pm 0.02 \text{ MHz per gauss}$ , the uncertainty is from the fitting of the peak positions in Fig. 1c. The single photon emission nature is further confirmed by the second-order correlation measurement presented in Supplementary Fig. 4a. Together with the zero-field splitting parameters  $D = 1340.4 \pm 1.3 \text{ MHz}$ ,  $E = 6.95 \pm 1.82 \text{ MHz}$ ,  $168.8 \pm 2.5 \text{ kcps}$  saturation intensity (Supplementary Fig. 4, the uncertainties arise from the fitting process), all these characteristics are consistent with PL6<sup>29</sup>. The small discrepancies between the D and E with the literature are attributed to the lateral and longitudinal strain of the thin film<sup>31</sup>. Subsequently, coherent control of the single PL6 electron spin has been demonstrated, as evidenced by the Rabi oscillation and Ramsey fringes displayed in Fig. 1d,e, respectively. From the fitting, the

inhomogeneous spin-dephasing time  $T_2^*$  is extracted to be  $460 \pm 35 \text{ ns}$ . The longitudinal relaxation time  $T_1$  is measured to be  $146 \pm 44 \mu\text{s}$  (Supplementary Fig. 4), similar to those in bulk materials<sup>29</sup>. The coherence time  $T_2$  is measured to be  $4.62 \pm 1.65 \mu\text{s}$  (Supplementary Fig. 4), lower than  $23.2 \mu\text{s}$  in the bulk material<sup>29</sup>. The coherence time is influenced by various factors like isotopic composition in the solid, surface treatment methodologies, and the ion implantation processes. The sample we used in this work is a primitive commercial SiC wafer. The coherence time can be effectively extended through the application of dynamical decoupling techniques<sup>32</sup> and isotopic engineering<sup>21</sup>.

### Coherent control of single nuclear spins on SiCOI

Nuclear spins are crucial resources in defect-based quantum technologies. Based on the controlled generation and coherent control of a single PL6 spin, we proceed to nuclear spin manipulation and initialization. In natural SiC, ~1% of the carbon atoms ( $^{13}\text{C}$ ) and 4.7% of silicon atoms ( $^{29}\text{Si}$ ) possess nuclear spins with  $I = 1/2$ . Strong coupling occurs when the nuclear spin resides within several lattice sites of PL6. The hyperfine interaction can exceed both the electron and nuclear spin dephasing rates  $1/T_2^*$ . This strong coupling is valuable for implementing fast gate operations and high-speed quantum memories<sup>33</sup>. We successfully identified an electron-nuclear spin-coupled system PL6 B in the sample, as shown in Fig. 2a. The single PL6 electron spin is strongly coupled to a first shell  $^{13}\text{C}$  nuclear spin<sup>33</sup>. We use  $0, \pm 1$ , and  $\uparrow, \downarrow$  to denote the electron and nuclear spin, respectively. The full Hamiltonian of the system can be written as

$$H = D \cdot [S_z^2 - S(S+1)/3] + \gamma_e \mathbf{B} \cdot \mathbf{S} + \mathbf{S} \cdot \mathbf{A} \cdot \mathbf{I} - \gamma_{^{13}\text{C}} \mathbf{B} \cdot \mathbf{I} \quad (1)$$

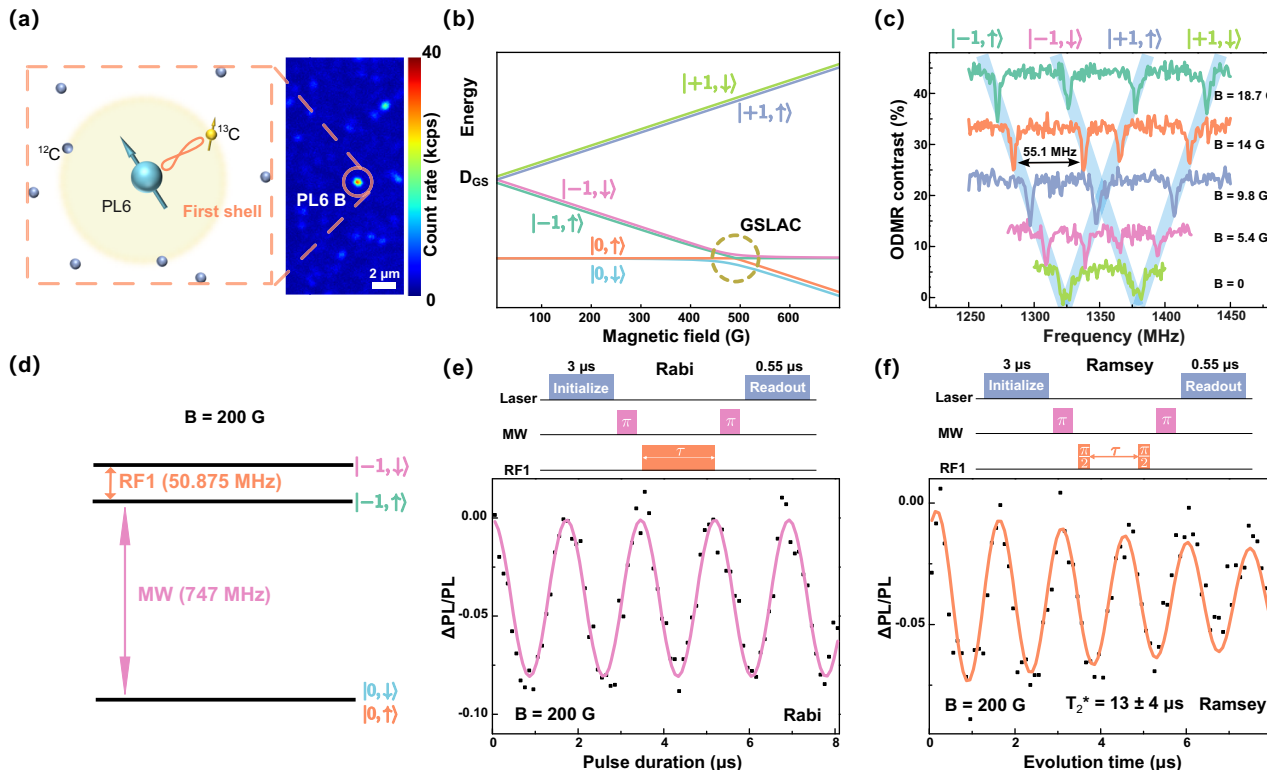


**Fig. 2 | Coherent control of single  $^{13}\text{C}$  nuclear spins coupled with PL6 B on SiCOI.** a An illustration of a single PL6 electron spin coupled with a  $^{13}\text{C}$  nuclear spin in the first shell. b The energy diagram of ground state spin sublevels as a function of c-axis magnetic field B. GSLAC is marked with a dashed circle. We use  $0, \pm 1$ , and  $\uparrow, \downarrow$  to denote the electron and nuclear spin, respectively. c ODMR spectra of the PL6 B electron spin coupled with the first shell  $^{13}\text{C}$  nuclear spin from 0 G to 18.7 G. The pale blue lines indicate the change of different peaks with the magnetic field. The slope is  $2.82 \pm 0.03 \text{ MHz/G}$ , corresponding to a c-axis defect's Zemman splitting.

d Simplified representation of the energy levels of the electron-nuclear coupled system at  $B = 200 \text{ G}$ .  $|0, \uparrow\rangle$  and  $|0, \downarrow\rangle$  are degenerate. e Rabi and f Ramsey of the  $^{13}\text{C}$  nuclear spin under 0.1 mW excitation. Their pulse sequences contain laser initialize, MW  $\pi$ -pulse, and RF1  $\pi$ -pulse or  $\pi/2$ -pulse. MW and RF1 are the pulses that drive  $|0, \uparrow\rangle$  to  $| -1, \uparrow\rangle$  and  $| -1, \uparrow\rangle$  to  $| -1, \downarrow\rangle$  respectively. Each cycle is repeated around 10 million times to reduce the measurement error. The nuclear spin is mapped and read out through the electron spin. The Ramsey fringe is fitted with a cosine exponential decay function, yielding a  $T_2^* = 13 \pm 4 \mu\text{s}$ .

Here,  $D$  represents the zero-field splitting parameter of the electron spin,  $S$  and  $I$  are the electron spin-1 and nuclear spin-1/2 operators, respectively.  $\gamma_e = 2.8 \text{ GHz T}^{-1}$  is the electron-spin gyromagnetic ratio.  $\gamma^{13}\text{C} = 10.708 \text{ MHz T}^{-1}$  is the gyromagnetic ratio of  $^{13}\text{C}$  nuclear spin.  $A$  is the hyperfine-interaction tensor between PL6 and  $^{13}\text{C}$ . When the nuclear spin resides in the first shell, the electron-nuclear spin coupling is strong enough to split the ground state energy levels. Two distinct, individually addressable transitions in SiC, separated by  $-55.1 \pm 0.6 \text{ MHz}$  are identified. These transitions correspond to the  $\uparrow$  and  $\downarrow$  nuclear spin states, observed without an external magnetic field. The hyperfine interaction strength varies drastically depending on their position in the lattice. We attribute this huge hyperfine splitting to coupling with a carbon isotope nuclear spin  $^{13}\text{C}$  in the first shell<sup>34</sup>. When a c-axis magnetic field is added,  $m_s \pm 1$  are no longer degenerates and split at a slope of  $2.82 \text{ MHz/G}$  due to Zeeman splitting, as shown in Fig. 2b, c. The ground-state spin-level anticrossings (GSLAC) region is marked with a dashed circle.

We chose a  $B$  field at around  $200 \text{ G}$  between the GSLAC point and zero fields to resolve the four transitions well for the following coherent control. The simplified representation of the energy levels of the electron-nuclear coupled system at  $B = 200 \text{ G}$  is depicted in Fig. 2d. Since it is far away from the GSLAC point,  $|0, \uparrow\rangle$  and  $|0, \downarrow\rangle$  are degenerate. There is no nuclear spin polarization at this  $B$  field, so the nuclear spin must be mapped to the electron spin before control and readout, as the control sequence depicted in Fig. 2e, f. The frequency of RF1 corresponds to the energy gap between  $| -1, \uparrow\rangle$  and  $| -1, \downarrow\rangle$ . The electron spin is first prepared in the  $m_s = -1$  state, and an RF pulse is used to drive nuclear Rabi oscillations (Fig. 2e) and Ramsey fringes (Fig. 2f). The Ramsey fringes yield a pure dephasing time of  $13 \pm 4 \mu\text{s}$ . The observed pure dephasing time  $T_2'$  of  $13 \mu\text{s}$  is notably shorter than the millisecond range<sup>35</sup>, and the sustained Rabi oscillations lasting up to  $8 \mu\text{s}$  without significant decay are also brief compared to the hundreds of microseconds<sup>14,21</sup>. This relatively short timescale can be attributed to the strong interaction with the environment through the electron spin<sup>36</sup>. It can, however, be significantly extended by selecting a nuclear spin not in the first shell or by decoupling the electron spin via the ionization process<sup>37</sup>. Furthermore, the SiC wafer used in our study is a basic commercial sample. Coherence times for both nuclear and electron spins can be effectively enhanced through dynamical decoupling techniques and isotopic engineering<sup>21</sup>. Besides a single  $^{13}\text{C}$  nuclear spin, a single  $^{29}\text{Si}$  nuclear spin has also been coherently controlled on SiCOI, as presented in Supplementary Note 3.

### Near-unity dynamic polarization of a single nuclear spin on SiCOI

In addition to coherent control, efficient initialization of the single nuclear spin memory is another critical capability in quantum information processing. Dynamical nuclear polarization (DNP) can effectively transfer electron spins to neighboring nuclei via hyperfine interaction<sup>19,38</sup>, serving as a basis for quantum memories and computing<sup>37,39</sup>, nuclear magnetic resonance sensitivity enhancement<sup>40</sup>, and solid-state nuclear gyroscopes<sup>3</sup>. We demonstrate that room-temperature DNP can be efficiently utilized on SiCOI, achieving a near-unity degree of polarization for a single nuclear spin. When the system is far from the anticrossing point, nuclear spins will not be optically polarized, and equal populations of  $|\pm 1, \uparrow\rangle$  and  $|\pm 1, \downarrow\rangle$  will result in the same intensity of the ODMR spectrum, as shown in Fig. 2c. Near GSLAC, in each optical cycle,  $|0, \downarrow\rangle$  may evolve into  $| -1, \uparrow\rangle$ , exchanging electron and nuclear polarizations. Subsequent optical cycles polarize  $| -1, \uparrow\rangle$  to  $|0, \uparrow\rangle$ . The whole process polarizes the nuclear spins simply by optical illumination<sup>19,38</sup>.

To uncover the detailed mechanism of the DNP near the GSLAC point, ODMR measurements at different magnetic fields have been conducted with a  $914 \text{ nm}$  off-resonant CW excitation as illustrated in

Fig. 3a. Our microwave source limits the lower bound of the microwave frequency to  $20 \text{ MHz}$ . Once the hyperfine tensor  $A$  is given, the energy separation between the electron and nuclear eigenstates can be calculated from the total Hamiltonian<sup>41,42</sup>. The most fitted results are presented with colored solid lines (with  $A_{xx} = A_{yy} = 93.1 \pm 0.3 \text{ MHz}$ ,  $A_{zz} = 56.5 \pm 0.2 \text{ MHz}$ ), where each color line represents a transition. Notably,  $| -1, \uparrow\rangle$  to  $|0, \uparrow\rangle$  maintains its intensity as the magnetic field approaches the anticrossing point. In contrast,  $| -1, \downarrow\rangle$  to  $|0, \uparrow\rangle$  weakens and vanishes from  $B = 460 \text{ G}$ , signifying where strong nuclear polarization occurs. The degree of nuclear spin polarization  $P$  is defined as  $(I^+ - I^-)/(I^+ + I^-)$ , where  $I^+$  and  $I^-$  denote the populations of the nuclear spins  $\uparrow$  and  $\downarrow$  respectively<sup>19,38</sup>. The populations are quantified by performing the Lorentzian fit of individual peaks. As illustrated in Fig. 3b, the solid lines are the theoretically calculated curve of  $\rho = \rho_\uparrow - \rho_\downarrow$  ( $\rho_\uparrow$  and  $\rho_\downarrow$  are the populations of nuclear spin up and down, see Methods). The maximum polarization degree achieved is  $0.98 \pm 0.04$ , reaching near-unity initialization of the single nuclear spin. To confirm this polarization, the ODMR spectra and Rabi oscillations near and far away from the GSLAC point are compared as represented in Fig. 3c–e. When  $B = 217 \text{ G}$ , the two ODMR spectra have similar contrast (Fig. 3c), the same as in Rabi oscillations (Fig. 3d). However, when  $B = 478 \text{ G}$  where the nuclear spin polarization is strong,  $| -1, \downarrow\rangle$  to  $|0, \uparrow\rangle$  vanishes in both ODMR spectra and corresponding Rabi oscillation (Fig. 3e, f).

### Optically detected nuclear magnetic resonance (ODNMR) and electron-nuclear entanglement generation

After performing complete control and near-unity polarization of a single nuclear spin, we have all the prerequisites to demonstrate the generation of an electron-nuclear entangled state of the PL6 B. The simplified energy level scheme of the electron-nuclear coupled system is depicted in Fig. 4a. MW ( $|0, \uparrow\rangle$  to  $| -1, \uparrow\rangle$ ) and RF2 ( $|0, \uparrow\rangle$  to  $|0, \downarrow\rangle$ ) in this subspace can be obtained directly from the ODMR measurements, while RF1 ( $| -1, \uparrow\rangle$  to  $| -1, \downarrow\rangle$ ) is missing due to the strong nuclear polarization near the GSLAC point, as also evident in Fig. 3a. To recover RF1, the pulse sequence in Fig. 4b is used after the system is optically initialized to  $| -1, \uparrow\rangle$ . The electron spin is prepared in the  $m_s = -1$  state and then an RF pulse is applied. The state is then read out by projecting onto the electron spin again. By varying the frequency of the RF pulse, the optically detected nuclear magnetic resonance (ODNMR) spectra are obtained as indicated in Fig. 4c. RF1 transition is extracted to be  $27.688 \pm 0.009 \text{ MHz}$  from the Lorentz fitting. After successfully addressing all three transitions, quantum state tomography (QST) can be conducted utilizing the MW as a working transition (see Supplementary Fig. 6, Supplementary Tables 1 and 2 for the details). The evolution of electron-nuclear states is tracked by performing quantum state tomography at different stages. First, the qubits are initialized by optical pumping due to nuclear spin pumping, after which quantum state tomography is performed. The measured density matrix is presented below the circuit in Fig. 4d with a fidelity of 0.98. This fidelity is the same as the degree of polarization obtained with the ODMR peak fitting method in the previous section, thus reconfirming the near-unity nuclear spin polarization. Next, a maximal superposition is created by applying two gates, as presented in Fig. 4d, entangling the electron and nuclear spin into one of the Bell states  $|\Psi^+\rangle = (|0, \uparrow\rangle + | -1, \downarrow\rangle)/\sqrt{2}$  (Fig. 4d). We successfully generated the electron-nuclear entanglement in this system with a fidelity of 0.89, estimated from the density matrix obtained through QST (see Methods and Supplementary Note Tables for details). Similar to PL6 B, PL6 C is another single electron spin with a strongly coupled first-shell  $^{13}\text{C}$  nuclear spin. The coupling strength is nearly  $56 \text{ MHz}$  as shown in Supplementary Fig. 10a. Both ODNMR and entanglement generation of this quantum register have been successfully demonstrated within the membrane, as illustrated in Supplementary Fig. 11.

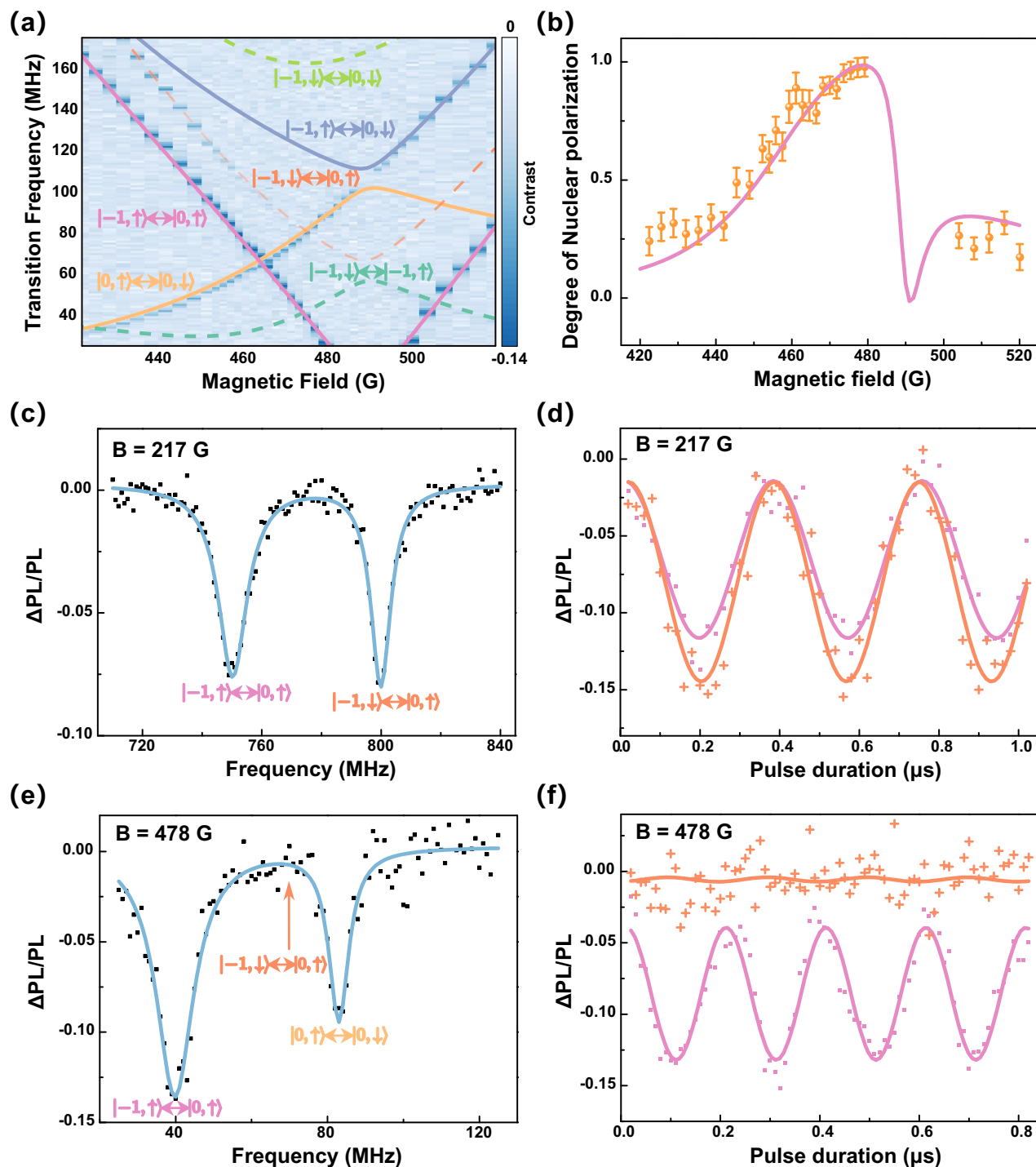


**Fig. 3 | Dynamic polarization of the single  $^{13}\text{C}$  nuclear spin (PL6 B) on SiCOI.** a ODMR spectra of the single PL6 defect coupled with single first-shell  $^{13}\text{C}$  nuclear spin at different magnetic fields near GSLAC. The vibrant lines are the theoretical calculation of the transition frequency of the spin sublevels with the total Hamiltonian (1).  $| -1, \uparrow \rangle \rightarrow | 0, \uparrow \rangle$  maintains its intensity as the magnetic field approaches the anticrossing point. In contrast,  $| -1, \downarrow \rangle \rightarrow | 0, \uparrow \rangle$  weakens and vanishes from  $B = 460$  G, signifying where strong nuclear polarization occurs. b The degree of nuclear spin polarization is defined by  $P = (I^+ - I^-)/(I^+ + I^-)$ , and  $I^+$  and  $I^-$  are extracted

from the Lorentzian fitting of the ODMR spectra in (a). The maximum polarization degree is  $0.98 \pm 0.04$ . The error bars are propagated from the standard deviations of parameters in the Lorentzian fitting. c and e ODMR spectra recorded for  $B = 217$  G (away from GSLAC and no obvious nuclear polarization) and  $B = 478$  G (at GSLAC where nuclear polarization is strong). The peaks correspond to transitions  $| -1, \uparrow \rangle \leftrightarrow | 0, \uparrow \rangle$  and  $| -1, \downarrow \rangle \leftrightarrow | 0, \uparrow \rangle$  respectively. d & f Rabi oscillations of the transitions in (c) & (e).

### Deterministic integration of the entangled quantum register into a waveguide

A critical step for developing SiCOI quantum photonics platforms is integrating single divacancy spins or quantum registers into photonic circuits and realizing on-chip integrated quantum photonic devices.

We have achieved this goal by further developing a nanoscale positioning technique<sup>43</sup> via direct camera imaging and pattern recognition (Supplementary Fig. 3). With this technique, the positioning accuracy of a single quantum register has been honed close to 10 nm, enabling the precise design and realization of surrounding photonic structures

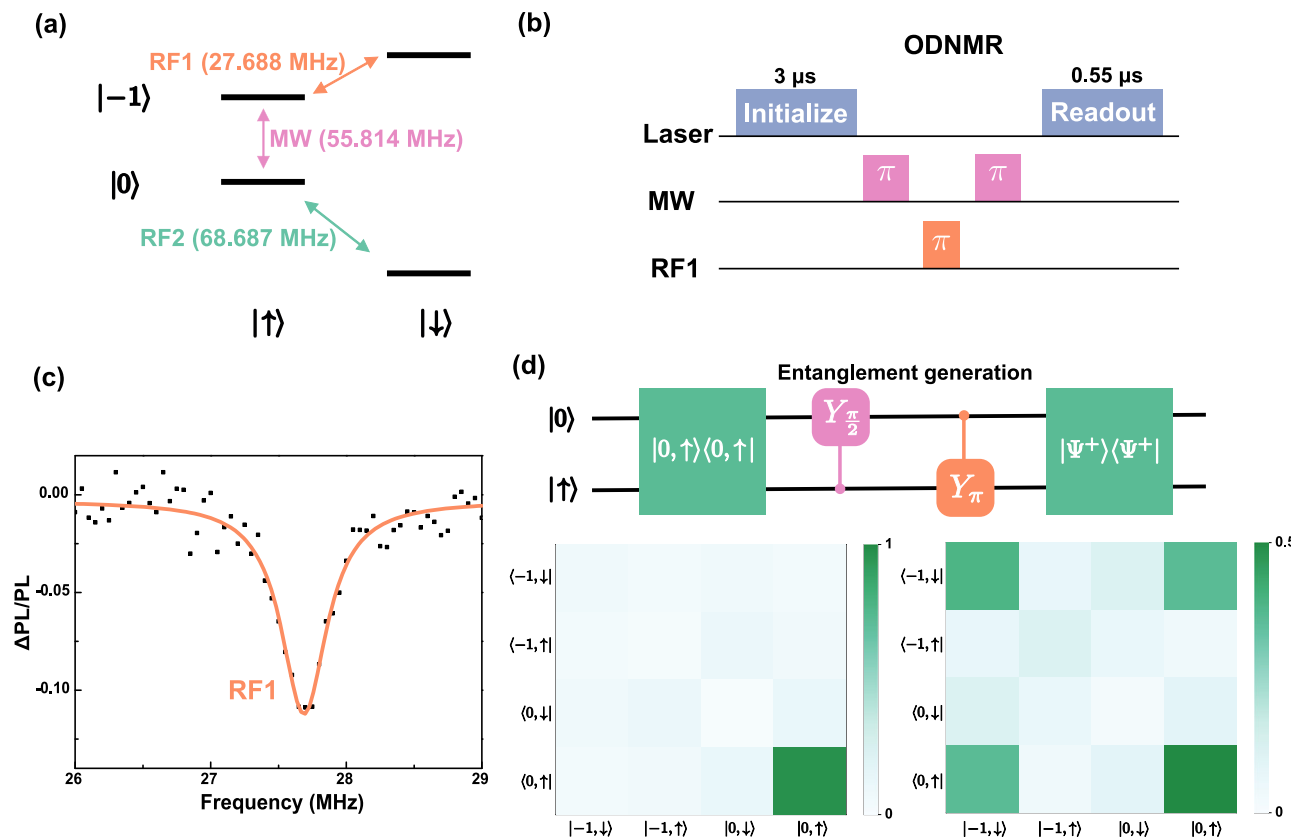


**Fig. 4 | Optically detected nuclear magnetic resonance (ODNMR) and entanglement generation of PL6 B.** **a** Simplified energy level scheme of the electron-nuclear coupled system. MW, RF1, and RF2 are three addressable transitions. MW and RF2 can be obtained directly from the ODMR spectra, while RF1 is missing due to the strong nuclear polarization. To recover RF1, the pulse sequence in **(b)** is used

with the help of electron spin. **c** Optically detected nuclear magnetic resonance measurement with the sequence in **(b)**. **d** upper panel: Gate operation circuit diagram for the entanglement generation and state tomography. lower panel: density matrix from quantum state tomography of the initial ( $|0, \uparrow\rangle\langle 0, \uparrow|$ ) and entangled state ( $|\Psi^+\rangle\langle \Psi^+|$ ). The fidelity of the target state is 0.98 and 0.89, respectively.

for on-chip integration. To illustrate this potential, We have designed waveguides equipped with directional couplers that encase the PL6 C quantum register. The photonic nanostructures are then fabricated with a combined process of electron beam lithography and reactive ion etching (Methods). The inset in Fig. 5a shows the top-view scanning electron microscope image of one waveguide, and all the structural parameters match the design very well.

The quantum register was optically characterized by scanning the waveguide confocally. A bright emission spot can be clearly seen in Fig. 5b. Since the surrounding SiC has been completely etched away, we can confirm that the PL6 C quantum register is encased in the waveguide. By fixing the excitation beam on PL6 C, we changed the collection angle with a scanning mirror and recorded the angle-dependent emission, as depicted in Fig. 5c. Two additional emission spots can be observed at the positions of the grating couplers, indicating that the quantum register is integrated inside the waveguide and that its emission is being confined and guided by the nanostructures. Similarly, the spin properties of the quantum register in the photonic waveguide were examined. The ODMR spectrum under different magnetic B fields shows an apparent  $56.1 \pm 0.2$  MHz splitting (Fig. 5d), confirming the persistent coupling between the nuclear and electron spins.

Based on the successful integration, we compared the stability of photon emission before and after etching. The results are summarized in Fig. 5e as purple hollow rhombus (before integration) and cross (after integration). The photon emission was collected at intervals of 0.1 s over a duration of 300 s. It is easy to see that the emissions both before and after integration are stable, and no blinking or bleaching can be observed. Meanwhile, two characteristic Rabi oscillations (MW

transition) are shown in the same figure with green hollow rhombuses (before integration) and crosses (after integration), thus demonstrating that the register can be coherently controlled without degradation. The complementary experiments on spin properties (Supplementary Fig. 10) reveal that the  $T_1$  and  $T_2^*$  of the waveguide-integrated PL6 C are  $188 \pm 43$   $\mu$ s and  $0.94 \pm 0.17$   $\mu$ s, respectively, comparable to the values before the integration. All these results confirm that the quantum register has been coupled to the waveguide without compromising its spin or optical properties. We attribute this to the size of the waveguide's width, which is usually on the wavelength or subwavelength scale and far larger than the influence of surface noise sources (<100 nm)<sup>44</sup>.

With the established stability, we repeated the near-unity nuclear spin polarization and ODNMR (Supplementary Note 5) as conducted with PL6 B in the membrane before. Near the GSLAC point, we observed the same near-unity polarization as displayed in Supplementary Fig. 10b, achieving a maximum polarization degree of  $0.99 \pm 0.01$  from the peak fitting. Finally, a Bell state  $|\Psi^+\rangle = (|0, \uparrow\rangle + |1, \downarrow\rangle)/\sqrt{2}$  has been prepared. The corresponding density matrix is depicted in Fig. 5f, and the fidelity estimated from quantum state tomography is still as high as 0.88, which is similar to the value before integration. The raw data of the quantum state tomography are presented in Supplementary Table 3. Then, we confirm that the quantum register can be integrated into photonic structures without obvious degradation.

In addition to PL6 C, the single electron spin PL6 A has also been integrated into a waveguide with the same technique, as depicted in Supplementary Note 4. No discernible degradation in optical or spin properties has been observed after integration, underscoring the

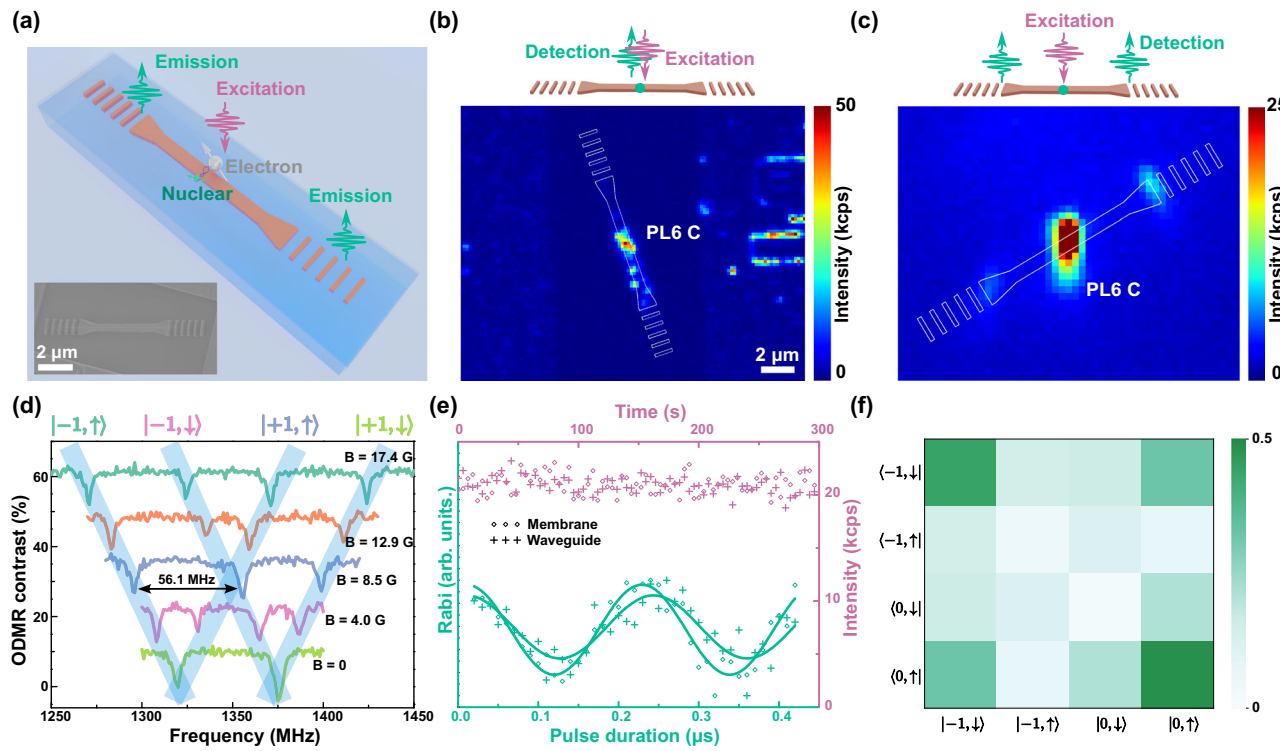


**Fig. 5 | Deterministic integration of the electron-nuclear quantum register PL6 C into waveguides.** **a** Schematic of the waveguide with two directional couplers, showing the quantum register at the center. Inset: Scanning Electron Microscope (SEM) image of the fabricated waveguides. **b** Confocal scan map of PL6 C after integration, with the outline of the waveguide included to guide the eye. **c** Collection angle-dependent scan map while PL6 C is excited. The central spot aligns with the defect, while the adjacent two spots are emissions from the directional couplers. The outline of the waveguide is included to guide the eye. **d** ODMR spectra of the waveguide-integrated PL6 C electron spin coupled with the first shell  $^{13}\text{C}$  nuclear spin in different magnetic B fields. The pale blue lines indicate the

change of different peaks with the magnetic field. The slope is  $2.79 \pm 0.01 \text{ MHz/G}$ , corresponding to the Zeeman splitting of a c-axis defect. The four transitions correspond to  $| -1, \uparrow \rangle$ ,  $| -1, \downarrow \rangle$ ,  $| 1, \uparrow \rangle$ , and  $| 1, \downarrow \rangle$ , respectively. The coupling strength is  $56.1 \pm 0.2 \text{ MHz}$ . **e** Comparison of photon stability ( $0.2 \text{ mW}$  CW excitation, with an interval of  $0.1 \text{ s}$  and duration of  $300 \text{ s}$ ) shown by purple hollow rhombuses (before integration) and crosses (after integration). Rabi oscillations (MW transition) are indicated by green hollow rhombus (before integration) and cross (after integration). **f** The density matrix of the generated Bell state with the quantum registers in a waveguide, showing a fidelity of  $0.88$  from quantum state tomography.

reliability of our approach. Our presented techniques are applicable to other photonic devices as well, e.g., beam splitters<sup>45</sup>, couplers, and micro rings. As a consequence, more complex quantum register-integrated on-chip quantum photonic circuits can be expected in the near future. Additionally, all single spins can be imaged in real-time using a commercial InGaAs CCD (Supplementary Video 1), enabling potential post-fabrication control of each quantum register in large-scale integration in the future.

## Discussion

SiCOI stands out for CMOS-compatible capabilities and hosting wealthily quantum registers. Our work demonstrates a critical step towards a SiC-based quantum photonic chip. We have successfully demonstrated single divacancy spin generation and nanoscale positioning on SiCOI. Using dynamical optical pumping near GSLAC, single nuclear spin polarization with a high degree of 98% has been experimentally demonstrated at ambient conditions. The coherent control of a single nuclear spin and an entangled state with a fidelity of 0.89 is achieved on the SiCOI as well. Based on the nanoscale positioning techniques, we have further integrated the entangled quantum register into SiC photonic waveguides for the first time and confirmed that all the optical and spin quantum characteristics are well preserved.

Our study contributes insights into developing on-chip quantum applications using SiC color centers. The on-chip integration approach may have advantages over bulks in both quantum sensing and quantum networks. For quantum sensing, on-chip routing in SiC photonic structures embeds quantum sensors, eliminating the need for top laser

exposure. Additionally, multi-node sensing<sup>39</sup> and enhanced sensitivity<sup>46</sup> can be achieved via photonic links and confinement. Nuclear spins in SiCOI also provide valuable sensors for nano-tesla magnetic sensing<sup>5</sup>, atomic nuclear spin imaging<sup>23</sup> and nuclear spin gyroscopes<sup>34</sup>. In the case of quantum networks, photonic integrated circuits also play a pivotal role. It offers photonic links for entangling remote spins via heralded protocols<sup>6,47</sup> and enhances light-matter interactions through various photonic crystal cavities<sup>48–52</sup>, vital to increasing the rate of entanglement generation. We believe that our work shall shed light on spin-photon entanglement generation<sup>53</sup>, remote entanglement of two or more SiC spins, and the eventual realization of multi-node quantum networks on a chip.

## Methods

### 4H-SiCOI and photonic devices fabrication

After the standard RCA cleaning, tens of nanometers thermal  $\text{SiO}_2$  was grown on a 4-in. 4H-SiC wafer with an epitaxy layer (The N-doping of the 4H-SiC wafer and epi-layer were  $1 \times 10^{18}$  and  $5 \times 10^{14} \text{ cm}^{-3}$ , respectively). Then the wafer and an oxidized Si substrate were activated with  $100 \text{ W O}_2$  plasma for 30 s. Then, the two wafers were bonded under the pressure of  $3000 \text{ N}$  at room temperature. Before the grinding process, the bonded structure was further annealed at  $800^\circ\text{C}$  for 6 h to enhance the bonding strength. The grinding process was divided into two steps. Firstly, the bonded wafer was treated with  $10 \mu\text{m}$  diamond slurry under the pressure of  $600 \text{ N}$  for about 10 h. The SiC layer was removed to about  $30 \mu\text{m}$  after that. Then, the SiC layer was further ground to a  $10 \mu\text{m}$  thickness with  $3 \mu\text{m}$  diamond slurry. The CMP

process was necessary to remove the damaged layer due to the grinding process. Finally, the SiCOI wafer was cut into dies and treated with ICP dry etching one by one for the final thickness adjustment. Etching SiC was done with 100 W RF and 1000 W ICP power under 10 mTorr. To fabricate single divacancy spins, hole arrays were patterned on the SiC layer using 180 nm thick PMMA (A4 with rotation speed 4000 rpm) as a photoresist through E-beam lithography. Following the 30 keV Carbon ion implantation with a dose of  $7.8 \times 10^{11} \text{ cm}^{-2}$ , the sample was annealed in a high vacuum at 900 °C for 30 min to remove residual lattice damage.

Photonic device fabrication began with the deposition of 30 nm Cr on SiCOI containing single spins surrounded by alignment cross markers (5 nm Ti and 50 nm Au). Then, the devices are patterned into an electron beam resist (ZEP 520A) via an electron beam lithography overlay process. After resisting development, the Cr mask is formed by ICP dry etching. The photonic devices are obtained under the Cr hard mask by ICP etching. Etching SiC was done with 100 W RF and 1000 W ICP power under 10 mTorr.

### Optical characterization and spin manipulation

Single defects were characterized by a home-built confocal microscope operating at room temperature. A 914 nm CW excitation laser within the range of optimal excitation wavelengths for VV<sup>0</sup>s<sup>54</sup> was focused on the single defect through a Nikon high numerical aperture oil objective (Model No.: CFI Plan Fluor 100X Oil). The fluorescence was finally counted by a superconducting nanowire single photon detector (SNSPD, Photon Technology) after passing a dichroic mirror (Semrock, Di02-R980-25 × 36) and a 1000 nm long-pass filter (Thorlabs, FELH1000). The SNSPD was replaced with an InGaAs CCD camera in the direct imaging system. All schematic diagrams of the setups are displayed in Supplementary Note 1. For the ODMR, Rabi, and Ramsey measurements, the microwave was generated using a synthesized signal generator (Mini-Circuits, SSG-6000 RC) and then gated by a switch (Mini-Circuits, ZASWA-2-50DR+). After amplification (Mini-Circuits, ZHL-25W-272+), the microwave signals were fed to a 20-μm-wide copper wire above the sample's surface. The excitation laser was modulated using an acoustic-optic modulator. The timing sequence of the electrical signals for manipulating and synchronizing the laser, microwave, and counter was generated using a pulse generator (SpinCore, PBESRPRO500). The external magnetic field was applied with a permanent magnet along the 4H-SiC c axis. Otherwise, the large transverse magnetic field may obscure the effect of the off-diagonal hyperfine elements. The strength of the magnetic field was adjusted by the distance of the magnet from the laser focus point on the sample. The magnetic field was determined precisely using ODMR spectrums from a single PL6 electron spin as a magnetometer.

### Single-defect imaging and nanoscale positioning

For positioning the PL6A single defect, a direct imaging system was used to acquire the defect array of single spins with the fabricated cross markers. Subsequently, the central highlight spot from unfiltered noise was removed by sigma clipping. After that, the processed image was cross-correlated with the ideal cross-mark pattern, and the peaks from the cross-correlation were extracted using Point Spread Function fitting, enabling us to acquire the transformed coordinates of the corresponding cross marks. We determined the coordinates of the single defect by employing Maximum Likelihood Estimation. This allowed us to ascertain the relative positional relationship between the single defect and the cross marks (Supplementary Note 1 and Supplementary Fig. 3 for more details).

### Probability of electron-nuclear spin flip-flop

The nuclear polarization P is related to the probability of electron-nuclear spin flip-flop, which can be calculated by the degree of mixing between spin and energy eigenstates. In our work, the probability of

nuclear spin up ( $\rho_{\uparrow}$ ) and down ( $\rho_{\downarrow}$ ) flips are calculated by relevant eigenstates<sup>41</sup>:

$$\rho_{\uparrow} = 4 \cdot |\langle 0, \downarrow | \beta \rangle|^2 \cdot [|\langle 0, \downarrow | \chi \rangle|^2 + |\langle 0, \downarrow | \delta \rangle|^2] + 4 \cdot |\langle 0, \downarrow | \delta \rangle|^2 \\ \cdot [|\langle 0, \downarrow | \alpha \rangle|^2 + |\langle 0, \downarrow | \chi \rangle|^2] \quad (2)$$

$$\rho_{\downarrow} = 4 \cdot |\langle 0, \uparrow | \alpha \rangle|^2 \cdot [|\langle 0, \uparrow | \chi \rangle|^2 + |\langle 0, \uparrow | \delta \rangle|^2] + 4 \cdot |\langle 0, \uparrow | \chi \rangle|^2 \\ \cdot [|\langle 0, \uparrow | \beta \rangle|^2 + |\langle 0, \uparrow | \delta \rangle|^2] \quad (3)$$

where  $|\alpha\rangle, |\beta\rangle, |\chi\rangle$  and  $|\delta\rangle$  are the eigenstates of Hamiltonian. The projections onto the  $|0, \uparrow / \downarrow\rangle$  states of these eigenstates are affected by the off-diagonal hyperfine elements.

### Entanglement fidelity

To determine the entanglement fidelity, we compare the measured density matrix  $\rho$  with the ideal target density matrix  $\rho'$  using the following definition<sup>21</sup>:

$$F = \text{Tr}(\sqrt{\sqrt{\rho}\rho'\sqrt{\rho}}) \quad (4)$$

### Data availability

The data that support the findings of this study are included within the paper and its Supplementary Information file. Source Data are provided in this paper. Any other relevant data are available from the corresponding authors upon request. Source data are provided with this paper.

### Code availability

The codes used for plotting the data are available from the corresponding authors upon request.

### References

- Pompili, M. et al. Realization of a multinode quantum network of remote solid-state qubits. *Science* **372**, 259–264 (2021).
- Stas, P.-J. et al. Robust multi-qubit quantum network node with integrated error detection. *Science* **378**, 557–560 (2022).
- Jarmola, A. et al. Demonstration of diamond nuclear spin gyroscope. *Sci. Adv.* **7**, eabl3840 (2021).
- Soshenko, V. V. et al. Nuclear spin gyroscope based on the nitrogen vacancy center in diamond. *Phys. Rev. Lett.* **126**, 197702 (2021).
- Simin, D. et al. All-optical dc nanotesla magnetometry using silicon vacancy fine structure in isotopically purified silicon carbide. *Phys. Rev. X* **6**, 031014 (2016).
- Bernien, H. et al. Heralded entanglement between solid-state qubits separated by three metres. *Nature* **497**, 86–90 (2013).
- Hensen, B. et al. Loophole-free bell inequality violation using electron spins separated by 1.3 kilometres. *Nature* **526**, 682–686 (2015).
- Hermans, S. L. N. et al. Qubit teleportation between non-neighbouring nodes in a quantum network. *Nature* **605**, 663–668 (2022).
- Sipahigil, A. et al. An integrated diamond nanophotonics platform for quantum-optical networks. *Science* **354**, 847–850 (2016).
- Bersin, E. et al. Development of a Boston-area 50-km fiber quantum network testbed. *Phys. Rev. Applied* **21**, 014024 (2024).
- Shi, F. et al. Single-protein spin resonance spectroscopy under ambient conditions. *Science* **347**, 1135–1138 (2015).
- Falk, A. L. et al. Polytype control of spin qubits in silicon carbide. *Nat. Commun.* **4**, 1819 (2013).
- Widmann, M. et al. Coherent control of single spins in silicon carbide at room temperature. *Nat. Mater.* **14**, 164–168 (2015).

14. Babin, C. et al. Fabrication and nanophotonic waveguide integration of silicon carbide colour centres with preserved spin-optical coherence. *Nat. Mater.* **21**, 67–73 (2022).
15. Lukin, D. M., Guidry, M. A. & Vučković, J. Integrated quantum photonics with silicon carbide: challenges and prospects. *PRX Quantum* **1**, 020102 (2020).
16. Awschalom, D. et al. Development of quantum interconnects (quics) for next-generation information technologies. *PRX Quantum* **2**, 017002 (2021).
17. Christle, D. J. et al. Isolated electron spins in silicon carbide with millisecond coherence times. *Nat. Mater.* **14**, 160–163 (2015).
18. Anderson, C. P. et al. Five-second coherence of a single spin with single-shot readout in silicon carbide. *Sci. Adv.* **8**, eabm5912 (2022).
19. Falk, A. L. et al. Optical polarization of nuclear spins in silicon carbide. *Phys. Rev. Lett.* **114**, 247603 (2015).
20. Klimov, P. V., Falk, A. L., Christle, D. J., Dobrovitski, V. V. & Awschalom, D. D. Quantum entanglement at ambient conditions in a macroscopic solid-state spin ensemble. *Sci. Adv.* **1**, e1501015 (2015).
21. Bourassa, A. et al. Entanglement and control of single nuclear spins in isotopically engineered silicon carbide. *Nat. Mater.* **19**, 1319–1325 (2020).
22. Taminiau, TimHugo, Cramer, J., van der Sar, T., Dobrovitski, V. V. & Hanson, R. Universal control and error correction in multi-qubit spin registers in diamond. *Nat. Nanotechnol.* **9**, 171–176 (2014).
23. Ajoy, A., Bissbort, U., Lukin, M. D., Walsworth, RonaldLee & Cappellaro, P. Atomic-scale nuclear spin imaging using quantum-assisted sensors in diamond. *Phys. Rev. X* **5**, 011001 (2015).
24. Arrad, G., Vinkler, Y., Aharonov, D. & Retzker, A. Increasing sensing resolution with error correction. *Phys. Rev. Lett.* **112**, 150801 (2014).
25. Hirose, M. & Cappellaro, P. Coherent feedback control of a single qubit in diamond. *Nature* **532**, 77–80 (2016).
26. Lukin, D. M. et al. 4h-silicon-carbide-on-insulator for integrated quantum and nonlinear photonics. *Nat. Photonics* **14**, 330–334 (2020).
27. Guidry, M. A., Lukin, D. M., Yang, Ki, Youl, Trivedi, R. & Vučković, J. Quantum optics of soliton microcombs. *Nat. Photonics* **16**, 52–58 (2022).
28. Powell, K. et al. Integrated silicon carbide electro-optic modulator. *Nat. Commun.* **13**, 1851 (2022).
29. Li, Q. et al. Room-temperature coherent manipulation of single-spin qubits in silicon carbide with a high readout contrast. *Natl. Sci. Rev.* **9**, nwab122 (2022).
30. Ivády, V. et al. Stabilization of point-defect spin qubits by quantum wells. *Nat. Commun.* **10**, 5607 (2019).
31. Falk, A. L. et al. Electrically and mechanically tunable electron spins in silicon carbide color centers. *Phys. Rev. Lett.* **112**, 187601 (2014).
32. De Lange, G., Wang, Zhi-Hui, Riste, D., Dobrovitski, V. V. & Hanson, R. Universal dynamical decoupling of a single solid-state spin from a spin bath. *Science* **330**, 60–63 (2010).
33. Rao, K. RamaKoteswara & Suter, D. Characterization of hyperfine interaction between an nv electron spin and a first-shell c13 nuclear spin in diamond. *Phys. Rev. B* **94**, 060101 (2016).
34. Son, N. T. et al. Divacancy in 4h-sic. *Phys. Rev. Lett.* **96**, 055501 (2006).
35. Maurer, PeterChristian et al. Room-temperature quantum bit memory exceeding one second. *Science* **336**, 1283–1286 (2012).
36. Mizuochi, N. et al. Coherence of single spins coupled to a nuclear spin bath of varying density. *Phys. Rev. B* **80**, 041201 (2009).
37. Dutt, M. V. Gurudev et al. Quantum register based on individual electronic and nuclear spin qubits in diamond. *Science* **316**, 1312–1316 (2007).
38. Jacques, V. et al. Dynamic polarization of single nuclear spins by optical pumping of nitrogen-vacancy color centers in diamond at room temperature. *Phys. Review Lett.* **102**, 057403 (2009).
39. Cai, M. et al. Parallel optically detected magnetic resonance spectrometer for dozens of single nitrogen-vacancy centers using laser-spot lattice. *Rev. Sci. Instrum.* **92**, 045107 (2021).
40. Giovannetti, V., Lloyd, S. & Maccone, L. Advances in quantum metrology. *Nat. Photonics* **5**, 222–229 (2011).
41. Wang, Hai-Jing et al. Sensitive magnetic control of ensemble nuclear spin hyperpolarization in diamond. *Nat. Commun.* **4**, 1940 (2013).
42. Ivády, V. et al. Theoretical model of dynamic spin polarization of nuclei coupled to paramagnetic point defects in diamond and silicon carbide. *Phys. Rev. B* **92**, 115206 (2015).
43. Liu, S., Srinivasan, K. & Liu, J. Nanoscale positioning approaches for integrating single solid-state quantum emitters with photonic nanostructures. *Laser Photonics Rev.* **15**, 2100223 (2021).
44. Sangtawesin, S. et al. Origins of diamond surface noise probed by correlating single-spin measurements with surface spectroscopy. *Phys. Rev. X* **9**, 031052 (2019).
45. Wang, Xu-Dong et al. Waveguide-coupled deterministic quantum light sources and post-growth engineering methods for integrated quantum photonics. *Chip* **1**, 100018 (2022).
46. Castelletto, S. et al. Silicon carbide photonics bridging quantum technology. *ACS Photonics* **9**, 1434–1457 (2022).
47. Nemoto, K. et al. Photonic architecture for scalable quantum information processing in diamond. *Phys. Rev. X* **4**, 031022 (2014).
48. Riedel, D. et al. Deterministic enhancement of coherent photon generation from a nitrogen-vacancy center in ultrapure diamond. *Phys. Rev. X* **7**, 031040 (2017).
49. Bracher, D. O., Zhang, X. & Hu, E. L. Selective purcell enhancement of two closely linked zero-phonon transitions of a silicon carbide color center. *Proc. Natl. Acad. Sci.* **114**, 4060–4065 (2017).
50. Lukin, D. M. et al. Two-emitter multimode cavity quantum electrodynamics in thin-film silicon carbide photonics. *Phys. Rev. X* **13**, 011005 (2023).
51. Crook, A. L. et al. Purcell enhancement of a single silicon carbide color center with coherent spin control. *Nano Lett.* **20**, 3427–3434 (2020).
52. Soref, R. & De Leonardi, F. Classical and quantum photonic sources based upon a nonlinear gap/si-superlattice micro-ring resonator. *Chip* **1**, 100011 (2022).
53. Gao, W. B., Fallahi, P., Togan, E., Miguel-Sánchez, J. & Imamoglu, A. Observation of entanglement between a quantum dot spin and a single photon. *Nature* **491**, 426–430 (2012).
54. Wolfowicz, G. et al. Optical charge state control of spin defects in 4h-sic. *Nat. Commun.* **8**, 1876 (2017).

## Acknowledgements

We thank Fazhan Shi, Jin Liu, and Gangqin Liu for the fruitful discussions. We acknowledge the support from the National Key R&D Program of China (Grant No. 2021YFA1400802, 2022YFA1404601, 2023YFB2806700), the National Natural Science Foundation of China (Grant No. 12304568, 12025402, 12334016, 62125501, 6233000076, 11934012, 62293520, 62293522, 62293521, 12074400 and 62205363), the GuangDong Basic and Applied Basic Research Foundation (Grant No. 2022A1515110382), Shenzhen Fundamental research project (Grant No. JCY20230807094408018), Guangdong Provincial Quantum Science Strategic Initiative (Grant No. GDZX2403004, GDZX2303001, GDZX2306002, GDZX2200001), Y.Z. acknowledges the support from the Young Elite Scientists Sponsorship Program by CAST, Q.S. acknowledges the support from the New Cornerstone Science Foundation through the XPLORE PRIZE, A.Y. acknowledges the support from the Shanghai Science and Technology Innovation Action Plan Program (Grant No. 22JC1403300) and CAS Project for Young Scientists in Basic Research (Grant No. YSBR-69), Z.L. acknowledges the support from the Major Key Project of PCL, the Talent Program of Guangdong Province (Grant No. 2021CX02X465).

## Author contributions

Y. Zhou and Q.S. conceived the idea. A.Y. and X.O. prepared the SiC membrane. H.H., Y. Zhang, Q. Luo, S.X., and Z.W. carried out the EBL lithography and SiC defect generation. Y. Zhou and H.H. built the setup and carried out the measurements. H.H., T.B., Y. Zhou, and Q.S. performed the simulations. Y. Zhou, H.H., Q. Li, D.L., C.L., and Z.L. contributed to the data analysis. All authors contributed to writing the paper.

## Competing interests

The authors declare no competing interests.

## Additional information

**Supplementary information** The online version contains supplementary material available at  
<https://doi.org/10.1038/s41467-024-54606-2>.

**Correspondence** and requests for materials should be addressed to Yu Zhou, Xin Ou or Qinghai Song.

**Peer review information** *Nature Communications* thanks the anonymous reviewers for their contribution to the peer review of this work. A peer review file is available.

**Reprints and permissions information** is available at  
<http://www.nature.com/reprints>

**Publisher's note** Springer Nature remains neutral with regard to jurisdictional claims in published maps and institutional affiliations.

**Open Access** This article is licensed under a Creative Commons Attribution-NonCommercial-NoDerivatives 4.0 International License, which permits any non-commercial use, sharing, distribution and reproduction in any medium or format, as long as you give appropriate credit to the original author(s) and the source, provide a link to the Creative Commons licence, and indicate if you modified the licensed material. You do not have permission under this licence to share adapted material derived from this article or parts of it. The images or other third party material in this article are included in the article's Creative Commons licence, unless indicated otherwise in a credit line to the material. If material is not included in the article's Creative Commons licence and your intended use is not permitted by statutory regulation or exceeds the permitted use, you will need to obtain permission directly from the copyright holder. To view a copy of this licence, visit <http://creativecommons.org/licenses/by-nc-nd/4.0/>.

© The Author(s) 2024